The 2025 World Congress on
Advances in Structural Engineering and Mechanics (ASEM25)
BEXCO, Busan, Korea, August 11-14, 2025

Analytical Model for Interface Slip in Steel-Concrete Composite Girders Under Moving Vehicle Loads

*Baolong Pang[1)], Ruihong Liang[2)] and Qingfei Gao[3)]

[1), 2), 3)] *School of Transportation Science and Engineering, HIT, Harbin, China*
[1)] baolong.pang@stu.hit.edu.cn
[2)] 24S032007@stu.hit.edu.cn
[3)] gaoqingfei@hit.edu.cn

ABSTRACT

The interface slip of steel-concrete composite (SCC) girders under moving vehicle loads is a critical factor influencing bridge durability. However, traditional models often oversimplify the dynamic interaction between slip degradation and vehicle-induced excitation. This study develops a analytical framework to predict dynamic slip behavior by integrating the energy variational principle with Euler-Bernoulli beam theory. The framework couples nonlinear interface slip stiffness with vehicle-bridge interaction dynamics. The vehicle is modeled as a mass-spring-damper system, while the SCC girder is represented as a simply supported beam with a partial shear connection. Key parameters, such as slip stiffness and vehicle speed, are systematically embedded into the governing equations, which are numerically solved using the Newmark-β method. Finite element modeling validates the proposed framework, demonstrating its capability to capture transient slip evolution during vehicle passage. Results indicate that slip stiffness is the primary factor influencing the dynamic response. Compared to traditional static methods, the model effectively accounts for time-dependent degradation effects, providing a more accurate dynamic prediction of interface slip. By improving the analysis and prediction of interface slip behavior, this work supports informed load-limiting decisions and helps prioritize maintenance strategies for aging infrastructure.

Keywords: Steel-concrete composite girders; Interface slip; Dynamic modeling; Moving loads

1. INTRODUCTION

Steel–concrete composite (SCC) structures have gained widespread application in bridge engineering due to their superior structural efficiency, rapid construction, and excellent fatigue resistance. By combining the compressive strength of concrete with the tensile capacity of steel, these systems achieve a high degree of composite action,

improving both strength and stiffness under service loads. However, this idealized behavior is often disrupted in real-world applications due to interface slip, which refers to the relative longitudinal displacement at the steel–concrete interface under loading (Nie and Cai, 2003). This phenomenon becomes particularly pronounced under moving vehicle loads, where dynamic effects, shear lag, and local bond deterioration accelerate slip progression and lead to a loss of composite action (Hou et al., 2015; Wang et al., 2024).

Numerous analytical and experimental studies have explored the interface behavior of SCC beams. Traditional beam theory assumes full interaction between the slab and girder, but this oversimplifies the real behavior where slip occurs at the interface, particularly under cyclic or dynamic loading. Early models addressed partial interaction using continuous or discrete shear spring formulations (Zhang et al., 2019; Ali et al., 2023), and extended these to include bond-slip relationships and fatigue deterioration under repeated loads (Suwaed and Karavasilis, 2020). Finite element models, employing contact elements or nonlinear connector formulations, have provided a more detailed perspective of localized slip and uplift phenomena (Wang et al., 2017; Hassanin et al., 2021).

Despite this progress, current methods often neglect the complex interaction between moving loads, road surface irregularities, and modal behavior of the girder. Vehicle-induced dynamic loads introduce significant vibrations and resonance effects, which amplify interface shear forces and induce high-frequency slip patterns (Guo et al., 2021; Gao et al., 2021). Studies have shown that road roughness and vehicle suspension properties significantly influence slip magnitudes and fatigue stress ranges (Guo et al., 2021; Zheng et al., 2023). Yet, limited research has been conducted on the space–time evolution of interface slip in SCC girders under such combined effects. Moreover, high-speed trains and multi-axle vehicles introduce repetitive impacts at intervals that coincide with the structure's natural frequencies, further exacerbating interface deterioration (Zhu et al., 2023; Zhang et al., 2021).

Recent efforts have introduced dynamic interaction models to capture these effects. For instance, Guo et al. (2021) developed a VBI framework integrating interface slip with multi-axial vehicle excitation, while Wang et al. (2024) proposed a space–time interface slip model validated through fatigue tests on prefabricated girders. However, these studies often rely on simplified assumptions such as linear slip models or neglect mode coupling in vibration response (Abdelkarim and ElGawady, 2016). In addition, there remains a gap in connecting the localized slip response with global performance metrics such as fatigue life, stiffness degradation, and serviceability loss (Sadeghi et al., 2020; Hassanin et al., 2021).

This study proposes a novel analytical framework to overcome these limitations. We integrate variational mechanics, high-order vibration analysis, and vehicle–bridge interaction under road roughness excitation to model the dynamic slip behavior in SCC girders. The shear connectors are modeled as continuous nonlinear springs, and the system is solved using Newmark-β integration to capture the temporal evolution of slip. Compared to existing approaches, our model accurately predicts the transient and spatial amplification of slip under multiple load passes and highlights critical regions prone to fatigue cracking. Additionally, we introduce a fatigue-sensitive slip index and damage localization metric to support decision-making in maintenance and monitoring

strategies.

The paper is organized as follows: Section 2 presents the theoretical model formulation, including coupling between the vehicle, bridge, and interface system. Section 3 validates the model using published experimental and numerical benchmarks. Section 4 provides a comprehensive parametric study examining the influence of shear stiffness, vehicle type, and surface conditions on dynamic slip responses. Section 5 concludes with engineering implications and proposes future research directions.

2. METHOD

2.1 *Energy Variational Method*

A functional is an extension of the concept of a function. Given a set of functions $f_i(x),\ i=1,2,3...n$ that form a function set C, and a set S of real numbers, if for each element $f_i(x)\in C$, there exists a corresponding element $J\in S$, then J is called the functional of $f_i(x)$, denoted by $J[f]$. In other words, a functional is a "function of a function," and its mathematical form can be expressed as:

$$J[f]=\int_{x_0}^{x_1} F\left(f,\dot{f},x\right)\mathrm{dx} \tag{1}$$

where, the function f is a function of x, $\dot{f}$ is the derivative of f with respect to x, and $[x_0,x_1]$ is the domain of definition for both f and $\dot{f}$. The functional form of the function F is known. When the form of the function f changes, the value of the functional $J[f(x)]$ will also change. A functional describes the relationship between a function and a variable.

Let $J[f(x)]$ be a continuous functional, and the function $f(x)$ is also referred to as a dependent variable (or functional variable). For any curve $f_0(x)$ taken from the set C, the variation of $f_0(x)$ at the function $f(x)$ is given by:

$$\delta f=f_0(x)-f(x) \tag{2}$$

Since δf exists, it will inevitably cause a change in the value of the functional. Here, we denote this as $J(f+\delta f)$. Then, the variation of the functional is defined as follows:

$$\Delta J(f)=J(f+\delta f)-J(f)=L(f,\Delta f)+r(f,\Delta f) \tag{3}$$

where $L(f,\Delta f)$ is a linear and continuous functional of δf, and $r(f,\Delta f)$ is a higher-order infinitesimal of δf. Then $\delta J=L(f,\Delta f)$ is called the variation of the functional $J[f]$.

2.2 Euler–Bernoulli girder dynamic model

In the Cartesian coordinate system XOY, the left end of the Euler–Bernoulli girder is taken as the origin. The function $w(x,t)$ represents the displacement caused by

system vibration, i.e., the vibration-induced deflection. $d(t)$ denotes the external disturbance acting at the right boundary of the girder, while $u(t)$ is the control input applied at the right end of the girder. L is the length of the Euler–Bernoulli girder, EI denotes its flexural rigidity, and T is the axial tension coefficient. m_s represents the mass of the load attached to the right boundary, and ρ is the mass per unit length of the Euler–Bernoulli girder. The kinetic energy of the Euler–Bernoulli girder is then given by:

$$E_k(t) = \frac{1}{2}\rho\int_0^l \dot{w}^2 dx + \frac{1}{2}m_s[\dot{w}(l,t)]^2 \tag{4}$$

where $\frac{\partial w(x,t)}{\partial t} = \dot{w}$, $\dot{w}(l,t)$ denotes the first derivative of $w(l,t)$ with respect to time at $x = l$. The kinetic energy of the system consists of two parts: one part is the kinetic energy of the Euler–Bernoulli girder, and the other is the kinetic energy of the boundary load at the right end of the system.

The total potential energy of the Euler–Bernoulli girder system includes the energy associated with axial tension and the bending strain energy of the system. It is given by:

$$E_p(t) = \frac{1}{2}T\int_0^l (w')^2 \mathrm{dx} + \frac{1}{2}EI\int_0^l (w'')^2 \mathrm{dx} \tag{5}$$

where, $\frac{\partial^2 w(x,t)}{\partial x^2} = w''$.

During the motion of the Euler–Bernoulli girder system, the virtual work done by external disturbances is given by:

$$\delta W_1(t) = d(t)\delta w(l,t) \tag{6}$$

where, $\delta w(l,t)$ denotes the vibration-induced displacement at the right boundary of the system, and δ represents the variational symbol. The virtual work done by the boundary control input on the system is given by:

$$\delta W_2(t) = u(t)\delta w(l,t) \tag{7}$$

Therefore, the total virtual work done by non-conservative forces on the Euler–Bernoulli girder system is given by:

$$\delta W(t) = d(t)\delta w(l,t) + u(t)\delta w(l,t) \tag{8}$$

According to Hamilton’s principle and the assumption of small displacements, the variation of the system's total energy over any arbitrary time interval is zero. Therefore, Hamilton’s principle can be expressed as:

$$\int_{t_1}^{t_2} \delta[E_k(t) - E_p(t) + W(t)]\mathrm{d}t = 0 \tag{9}$$

where $t_1 < t_2$, $t \in [t_1, t_2]$, and satisfy $\delta w(x,t_1) = \delta w(x,t_2) = 0$.

By applying the variational operation and integration by parts to Eq. (4), we obtain:

$$\int_{t_1}^{t_2} \delta E_k(t)dt = -m_s \int_{t_1}^{t_2} \ddot{w}(l,t)\delta w(l,t)dt - \rho \int_{t_1}^{t_2} \int_0^l \dot{w}\delta w dx dt \tag{10}$$

Similarly, by applying the variational operation and integration by parts to the potential energy term in Eq. (5), we obtain:

$$\begin{aligned} \int_{t_1}^{t_2} \delta E_p(t)dt = T\int_{t_1}^{t_2} w'(l,t)\delta w(l,t)dt + EI\int_{t_1}^{t_2} (w''\delta w')\Big|_0^l \, dt + EI\int_{t_1}^{t_2}\int_0^l w^{(4)}\delta w dx dt \\ -EI\int_{t_1}^{t_2} w^{(3)}(l,t)\delta w(l,t)dt - T\int_{t_1}^{t_2}\int_0^l w''\delta w dx dt \end{aligned} \tag{11}$$

where, $\frac{\partial w(x,t)}{\partial x} = w'$, $\frac{\partial^2 w(x,t)}{\partial x^2} = w''$, $\frac{\partial^3 w(x,t)}{\partial x^3} = w^{(3)}$, $\frac{\partial^4 w(x,t)}{\partial x^4} = w^{(4)}$.

For the total virtual work term, we have:

$$\int_{t_1}^{t_2} \delta W(t)dt = \int_{t_1}^{t_2} u(t)\delta w(l,t)dt + \int_{t_1}^{t_2} d(t)\delta w(l,t)dt \tag{12}$$

Substituting Eq. (10) – Eq. (12) into Eq. (9), the governing equation of the Euler–Bernoulli girder is obtained as:

$$\rho\ddot{w} + EIw^{(4)} - Tw'' = 0 \tag{13}$$

$\forall (x,t) \in (0,l] \times [0,+\infty)$, The boundary conditions of the system are given by:

$$\begin{cases} w'(0,t) = w''(l,t) = w(0,t) = 0 \\ m_s\ddot{w}(l,t) = u(t) + EIw^{(3)}(l,t) - Tw'(l,t) + d(t) \end{cases} \tag{14}$$

In summary, the Euler–Bernoulli girder model is represented by an infinite-dimensional partial differential equation coupled with an ordinary differential equation. Eq. (10) describes the dynamic characteristics of the system, while Eq. (14) illustrates the influence of the external disturbance $d(t)$ and the control input $u(t)$ on the vibration displacement $w(l,t)$ at the right boundary of the system.

2.3 Dynamic Model

When analyzing the dynamic performance of steel-concrete composite girders, the following fundamental assumptions are made: (1) Planar Motion: Only in-plane behavior is considered, with both concrete slab and steel girder assumed to be linear

elastic materials undergoing small deformations. (2) Euler-Bernoulli Girder Theory: Both components comply with Euler-Bernoulli girder assumptions (shear deformation and rotational inertia effects are neglected). (3) Interface Constraints: No vertical uplift (z-direction) occurs between concrete slab and steel girder. Only longitudinal relative slip along the x-axis is permitted at the interface. (4) Shear Connection: Bonding forces at the interface are neglected. All shear forces are transferred exclusively through shear connectors. Shear connectors are modeled as continuously distributed springs with equivalent stiffness K.

Based on these assumptions, the relationship between interface slip (u_{cs}) and axial displacements (u_c, u_s) as well as vertical displacement (w) is illustrated in Fig. 1, where w' denotes the first derivative of vertical displacement with respect to x.

As clearly shown in Fig. 1, the interface slip relationship can be expressed as:

$$u_{cs}(x,t) = u_c(x,t) - u_s(x,t) + h\frac{\partial w(x,t)}{\partial x} \tag{15}$$

where $h = h_c + h_s$.

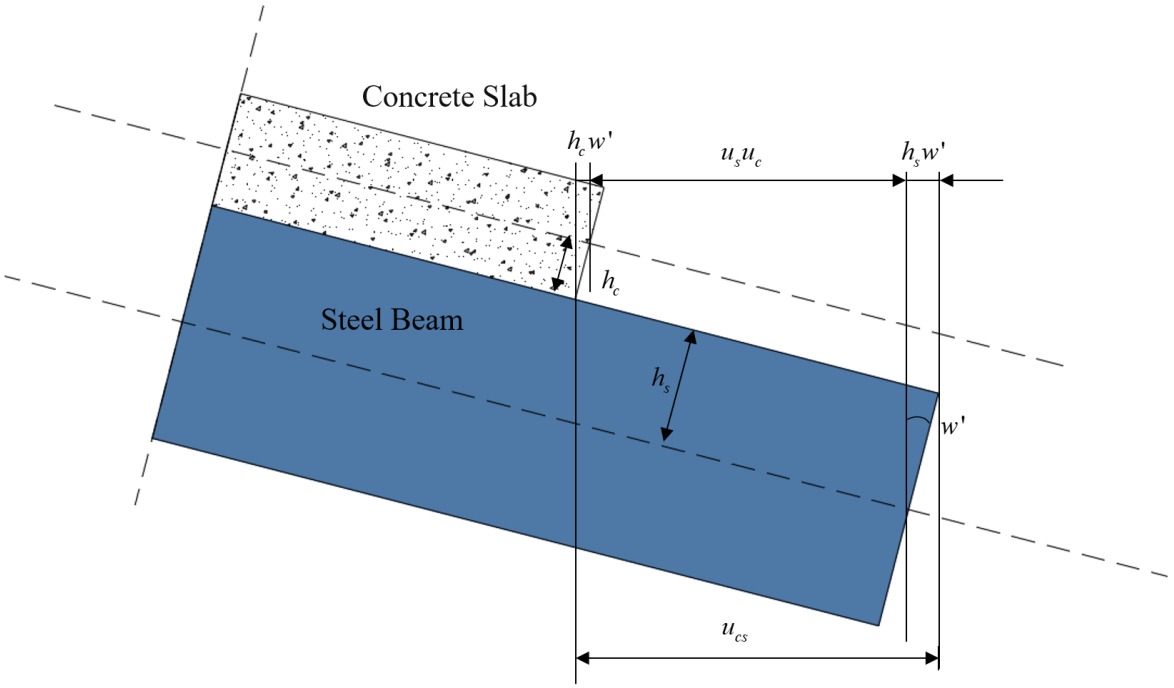

Fig. 1 Slip Relationship of Steel-concrete Composite Girders

The free vibration problem of steel-concrete composite girders can be described by Eq. (16) based on Hamilton's variational principle.

$$\delta\int_{t_1}^{t_2}\left(T - U - U_{cs}\right)\mathrm{d}t = 0 \tag{16}$$

where, T, U, and U_{cs} represent the kinetic energy of the composite girder, strain energy, and shear potential energy of the shear connectors, respectively.

The kinetic energy expression for the steel-concrete composite girder is given by:

$$T = \frac{1}{2}\sum_{i=c,s}\int_0^L \iint_S \rho_i \dot{w}^2 \mathrm{dSdx} = \frac{1}{2}\sum_{i=c,s}\int_0^L \rho_i A_i \dot{w}^2 \mathrm{dx} \tag{17}$$

where the superscript dot notation ("·") denotes the first derivative of the variable with respect to time (t), and dS represents the differential area element.

The strain energy expression for the steel-concrete composite girder is given by:

$$U = \frac{1}{2}\sum_{i=c,s}\int_0^L \int_s^t E_i \left(\frac{\partial u_i}{\partial x} - z_i \frac{\partial^2 w}{\partial x^2}\right)^2 dSdx \tag{18}$$

The potential energy expression for the shear connectors in steel-concrete composite girders is given by:

$$U_{cs} = \frac{1}{2}\int_0^L K u_{cs}^2 dx = \frac{1}{2}\int_0^L K\left(u_c - u_s + h\frac{\partial w}{\partial x}\right)^2 dx \tag{19}$$

By substituting Eq. (17)- Eq. (18) into Eq. (16) and performing variational calculus, the governing differential equations of motion for the steel-concrete composite girder can be derived as follows:

$$\delta u_c : E_c A_c \frac{\partial^2 u_c}{\partial x^2} - Kh\left(\theta + \frac{\partial w}{\partial x}\right) = 0 \tag{20}$$

$$\delta u_s : E_s A_s \frac{\partial^2 u_s}{\partial x^2} + Kh\left(\theta + \frac{\partial w}{\partial x}\right) = 0 \tag{21}$$

$$\delta w : m\ddot{w} + EI\frac{\partial^4 w}{\partial x^4} - Kh^2\left(\frac{\partial \theta}{\partial x} + \frac{\partial^2 w}{\partial x^2}\right) = 0 \tag{22}$$

The corresponding natural boundary conditions for the steel-concrete composite girder system are derived as follows:

$$N_c = E_c A_c \frac{\partial u_c}{\partial x} \tag{23}$$

$$N_s = E_s A_s \frac{\partial u_s}{\partial x} \tag{24}$$

$$M = EI\frac{\partial^2 w}{\partial x^2} \tag{25}$$

$$Q = K_s h^2 \left(\theta + \frac{\partial w}{\partial x} \right) - EI \frac{\partial^3 w}{\partial x^3} \tag{26}$$

where, M is the mass per unit length of the steel-concrete composite girder; EI is the algebraic sum of the flexural rigidity of sub-beams; θ is the rotation angle related to interfacial relative slip.

Combining Eq. (23) and Eq. (24) gives:

$$EA \frac{\partial^2 \theta}{\partial x^2} - K \left(\theta + \frac{\partial w}{\partial x} \right) = 0 \tag{27}$$

where $EA = \dfrac{E_c A_c \cdot E_s A_s \cdot h^2}{E_c A_c + E_s A_s}$ which can be defined as the slip flexural rigidity**.**

Combining Eq. (25) and Eq. (27) gives the final form of the governing differential equation for steel-concrete composite beams as follows:

$$\frac{\partial^6 w}{\partial x^6} - \frac{KEI_F}{EAEI} \frac{\partial^4 w}{\partial x^4} + \frac{m}{EI} \frac{\partial^4 w}{\partial x^2 \partial t^2} - \frac{mK}{EAEI} \frac{\partial^2 w}{\partial t^2} = 0 \tag{28}$$

where EI_F represents the sectional flexural rigidity under no-slip conditions (when shear connector stiffness is infinite).

Eq. (28) can be solved using the separation of variables method. The vertical vibration displacement $w(x,t)$ can be expressed as:

$$w(x,t) = \phi(x) \sin(\omega t + \varphi) \tag{29}$$

where $\phi(x)$ is the mode shape function of the vertical displacement $w(x,t)$ for the steel-concrete composite girder, $\sin(\omega t + \varphi)$ is the time-dependent modal amplitude, ω is the natural frequency of the composite girder, φ is the phase angle.

Substituting Eq. (29) into the governing differential Eq. (28) yields the decoupled motion equations of the steel-concrete composite girder:

$$\frac{d^6 \phi}{dx^6} - \frac{KEI_F}{EAEI} \frac{d^4 \phi}{dx^4} - \frac{m\omega^2}{EI} \frac{d^2 \phi}{dx^2} + \frac{mK}{EAEI} \omega^2 \phi = 0 \tag{30}$$

The characteristic equation corresponding to Eq. (30) is given by:

$$\lambda^6 - \frac{KEI_F}{EAEI} \lambda^4 - \frac{m\omega^2}{EI} \lambda^2 + \frac{mK}{EAEI} \omega^2 = 0 \tag{31}$$

where λ represents the eigenvalue of the governing differential equation.

Eq. (31) admits six solutions, namely $\pm\lambda_1$, $\pm\lambda_2$, and $\pm\lambda_3$ Consequently (Hou, 2013), the general solution to the governing differential Eq. (30) can be expressed as:

$$\phi(x) = A_1 \sin(\lambda_1 x) + A_2 \cos(\lambda_1 x) + A_3 \sinh(\lambda_2 x) + A_4 \cosh(\lambda_2 x) + A_5 \sinh(\lambda_3 x) + A_6 \cosh(\lambda_3 x) \quad (32)$$

From Eq. (23) to Eq. (26), it can be concluded that the steel-concrete composite girder has three displacement boundary conditions:

$$N = \frac{E_s A_s N_c - E_c A_c N_s}{E_s A_s + E_c A_c} = EA\left(\frac{\partial u_{cs}}{\partial x} - h\frac{\partial^2 w}{\partial x^2}\right) \quad (33)$$

$$M = EI\frac{\partial^2 w}{\partial x^2} \quad (34)$$

$$Q = K_s h^2\left(\theta + \frac{\partial w}{\partial x}\right) - EI\frac{\partial^3 w}{\partial x^3} \quad (35)$$

From Eq. (34) to Eq. (35) and the aforementioned governing differential equations, the boundary conditions for simply supported conditions are obtained as:

$$\phi(x) = 0 \quad (36)$$

$$\frac{d^2\phi(x)}{dx^2} = 0 \quad (37)$$

$$\frac{d^4\phi(x)}{dx^4} - \frac{m}{EI_F}\omega^2\phi(x) = 0 \quad (38)$$

Substituting the boundary conditions into Eq. (32) yields:

$$(\lambda_2^2 - \lambda_3^2)^2(\lambda_2^2 + \lambda_1^2)^2(\lambda_1^2 - \lambda_2^2)^2 \sin(\lambda_1 L)\sinh(\lambda_2 L)\sinh(\lambda_3 L) = 0 \quad (39)$$

Evidently, Eq. (39) holds true only when $\sin(\lambda_1 L) = 0$. This leads to the derivation of Eq. (40):

$$\lambda_1 = \frac{n\pi}{L} \quad (40)$$

Substituting $\lambda = \pm\lambda_{1i}$ into the characteristic Eq. (31) yields the natural frequencies and mode shapes of the steel-concrete composite girder.

2.4 Vehicle-Bridge Dynamic Interaction Model

The vehicle is simplified as a multi-degree-of-freedom rigid-body vibration system composed of spring-mass-damper elements, with the following assumptions:

(1) The chassis and axles are modeled as rigid bodies, forming a suspension system with spring-damper connections between the chassis and bridge deck;

(2) Vibrations of the vehicle body, suspension, and wheels in the longitudinal direction of the bridge deck are neglected;

(3) The vehicle body mass is concentrated at its center of gravity, wheel masses are concentrated at the axles, and the system exhibits lateral symmetry about the vehicle centerline;

(4) Wheel-to-deck contact points remain in continuous contact without separation.

The spring-mass vibration model is illustrated in Fig. 2, with vehicle model parameter values detailed in Reference (Gui, 2017). The vibration equations of the vehicle model can be written as:

$$M_v\ddot{z} + C_v\dot{z} + K_v z = F_v^{int} \tag{41}$$

where, M_v denotes the mass matrix of the vehicle system; C_v denotes the damping matrix of the vehicle system; K_v is the stiffness matrix of the vehicle system; F_v^{int} is t the inertial force vector acting on all degrees of freedom due to vehicle vibration; z denotes the state vector of the vehicle model, defined as: $z = \{z_1\, z_2\, z_3\, z_4\, z_5\, z_6\, z_b\, \theta_b\, \phi\}^{\mathrm{T}}$

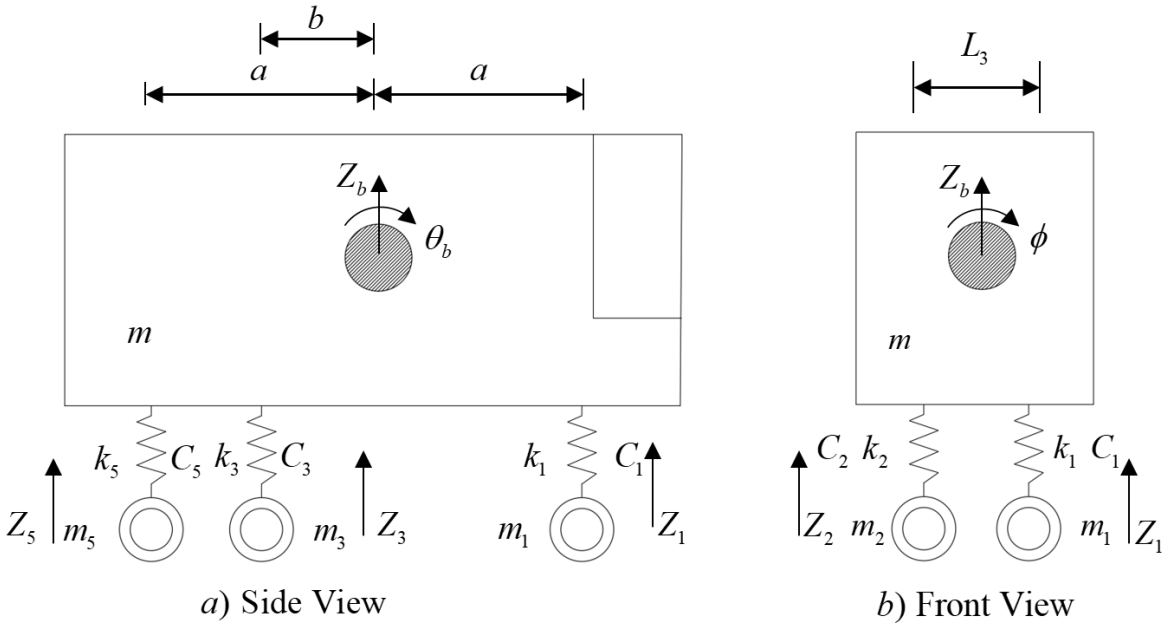

Fig. 2 Simplified vehicle model

2.5 Composite Girder Bridge Model

The steel-concrete composite girder model features spring connections and vertical coupling between the top surface of the steel girder and the bottom surface of the concrete slab at the stud locations. Each stud is simulated by two unidirectional spring elements to represent its longitudinal and transverse stiffness. Considering the actual loading conditions of a simply supported girder, the boundary constraints of the model are simplified as follows: at one end of the girder, translational degrees of freedom in the X, Y, and Z directions are restrained; at the other end, translational

degrees of freedom in the Y and Z directions are restrained, with the rotation about the transverse direction released at both ends. Modal data extraction is performed using the Block Lanczos method.

2.6 Road Roughness Simulation Methods

The road roughness simulation function is calculated using the harmonic superposition method, with the specific formula given in (17). In accordance with the power spectral density recommended in "Vehicle Vibration Input—Methods for Representing Road Roughness" (Xu, 2021), the statistical characteristics of road roughness are classified into eight grades, A to H, with their corresponding spatial density function detailed in Eq. (42).

$$\begin{cases} r(x,y)=\sum_{i=1}^{n} G(n_i)\cos(2\pi n_i\sqrt{x^2+y^2}+\varphi_i(x,y)) \\ G(n_i)=\sqrt{4G_q(n_i)\Delta n} \\ n_i=n_d+(i-0.5) \\ \Delta n(i=1,2,3...N)\Delta n=(n_u-n_d)/N \end{cases} \tag{42}$$

where, $G(n_i)$ represents the amplitude of the cosine function; $\varphi_i(x,y)$ denotes the random phase, whose value ranges between 0 and 2π; *x* and *y* correspond to the longitudinal and transverse coordinates of the road surface, *N* respectively is a sufficiently large positive integer; n_u and n_d are the upper and lower effective spatial frequencies of the road surface.

3. CASE STUDY

3.1 Bridge Summary

As shown in Fig. 3 and Fig. 4, the Honghu Lu Exit Ramp Bridge on the Harbin Third Ring Road features a three-span continuous configuration of 36 m + 50 m + 36 m. The structure employs a variable-depth steel-concrete composite twin single-cell box girder system with a quadratic parabolic soffit profile. Key dimensions include 4.2 m web spacing within each box, 2.5 m cantilever overhangs, girder heights of 2.8 m at intermediate supports and 2.0 m at midspan. Material specifications for structural components are provided in Table 1.

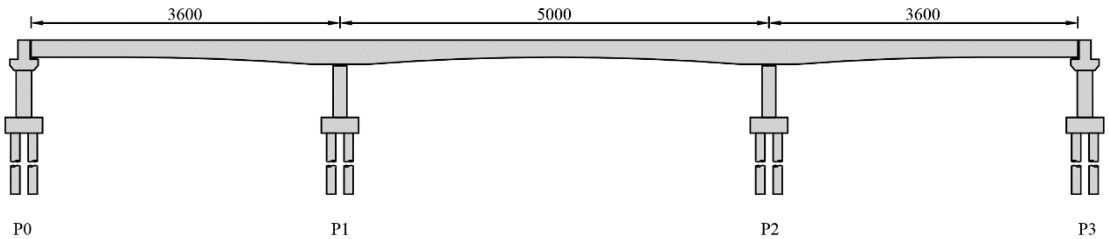

Fig. 3 Bridge General Layout

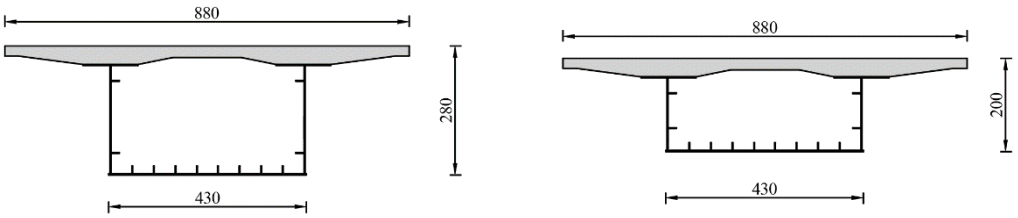

a) Support Section b) Midspan Section

Fig. 4 Bridge Cross-Section View

Table 1 Material Types for Various Bridge Components

Component	Material	Type
Bridge Deck	Concrete	C50
Bent Cap		C50
Pier Shaft		C40
Main Girder	Steel	Q345qE
Reinforcement		HRB335

3.2 Finite Element Model Setup

The finite element model was established by integrating the theoretical frameworks from Sections 2.4–2.6 to simulate the vehicle-bridge dynamic interaction. For the steel-concrete composite girder (Section 2.5), the concrete deck was modeled using SOLID65 elements with C50 material properties (elastic modulus 34.5 GPa, Poisson's ratio 0.2), while the steel girder employed SHELL181 elements with Q345qE steel properties (elastic modulus 206 GPa, Poisson's ratio 0.3). Shear connectors were simulated as COMBIN14 spring elements with equivalent stiffness:

$$K = \frac{n_{stud} \cdot k_{stud}}{L} \tag{43}$$

where n_{stud} is the total stud count and k_{stud} is the shear stiffness. L is the span length.

Simply supported boundary conditions were enforced: full translational fixation at the left support, and constrained Y/Z translations with released Y-axis rotation at the right support.

Vehicle-bridge coupling (Section 2.4) adopted a multibody system with parameters from Ref. (Hou, 2013): The tire-deck contact force was dynamically computed as:

$$F_v(t) = K_t \left[z_w(t) - w(x_v, t) - r(x_v) \right] \tag{44}$$

with $x_v = v \cdot t$ defining the vehicle position. Road roughness (Section 2.6) followed the ISO Grade B specification, generated via harmonic superposition.

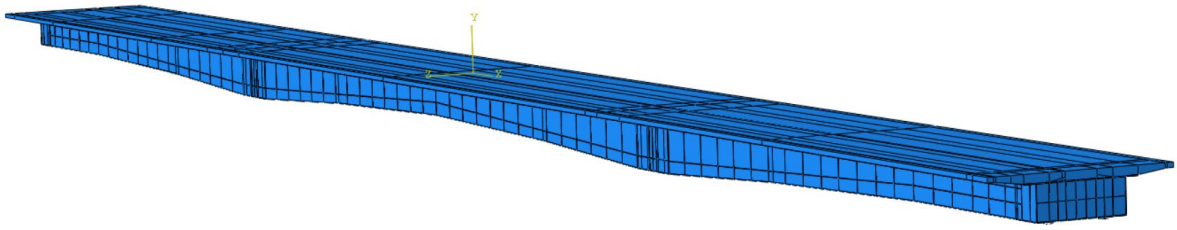

Fig. 5 Bridge model

3.3 Model Validation

The analytical framework's predictive capability was rigorously evaluated through dynamic vehicle-bridge interaction simulations. Validation focused on three critical aspects under a 30-ton vehicle traversing at 60 km/h with ISO-B road roughness:

(1) Modal Frequency Verification

Natural frequencies from analytical solutions and FEM showed close alignment (Table 2), with maximum errors $\leqslant$2.9% for the first two bending modes. This confirms accurate representation of system mass/stiffness distributions.

Table 2 Natural frequency comparison

Mode	Analytical (Hz)	FEM (Hz)	Error (%)
1	2.35	2.41	2.5
2	9.44	9.18	2.8
3	15.27	15.60	2.1
4	22.91	23.45	2.3
5	28.33	29.18	2.9

(2) Time-History Response Verification

Midspan Displacement: Analytical and FEM profiles showed strong correlation (R^2=0.96) with peak deviation of 4.1% at t=1.84 s (Fig. 6)

Analytical and finite element method (FEM) profiles for midspan displacement exhibited strong correlation (R^2 = 0.96), with a peak deviation of 4.1% occurring at t = 1.84 s (Fig. 6a). Interface slip comparisons at the L/4 section (Fig. 7) revealed a 6.8% peak value discrepancy during rear-axle crossing events, while maintaining a phase lag below 0.02 s throughout the vehicle passage. Both analytical and FEM results demonstrated consistent high-frequency response (>20 Hz), corresponding to vibrational Modes 3–5 of the composite structure.

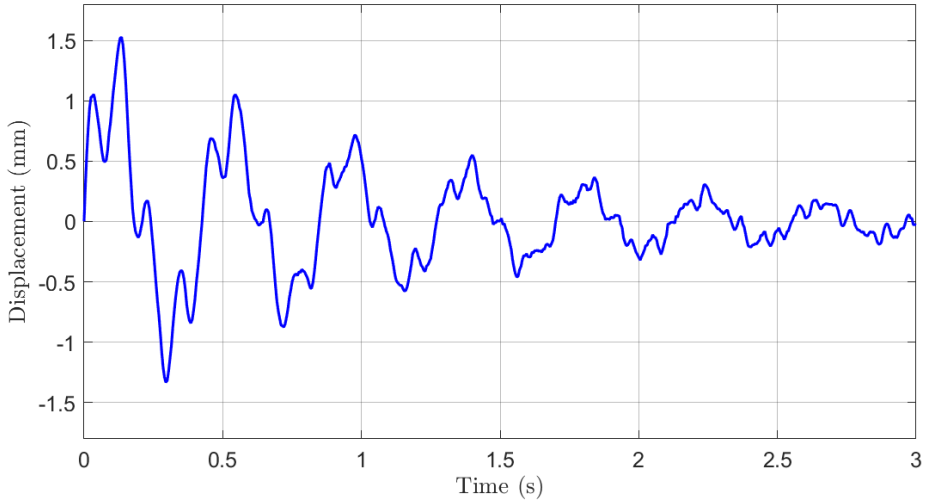

Fig. 6 Midspan Displacement Time History

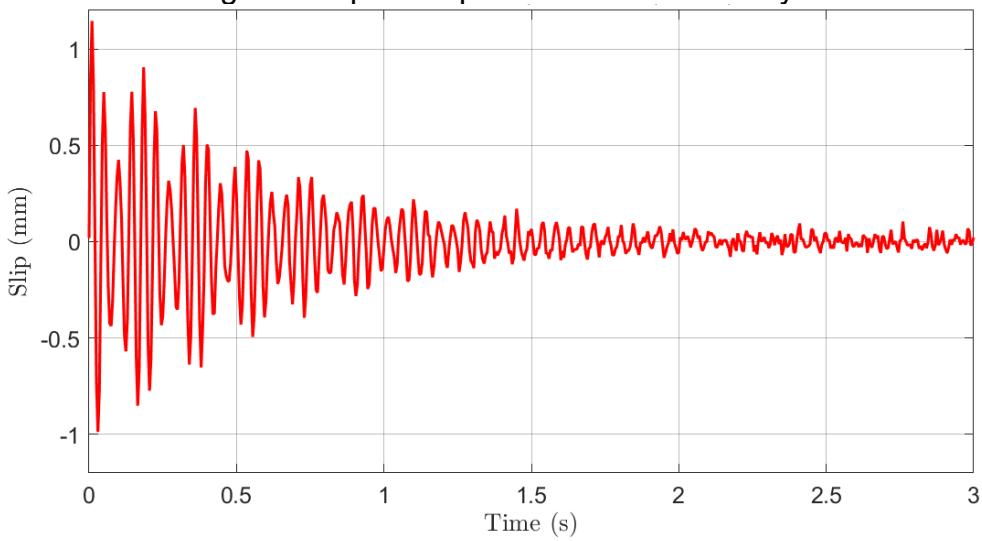

Fig. 7 Interface Slip at *L*/4 Section

(3) Higher-Mode Slip Localization

Spatiotemporal slip distributions (Fig. 8) revealed distinct modal contributions: Modes 1–2 governed global slip patterns with peak magnitudes at supports, while Modes 4–5 induced localized slip oscillations near midspan characterized by 5–8 mm wavelengths. Notably, Modes 7–8 generated high-frequency ripple effects (wavelengths <3 mm) during vehicle exit events.

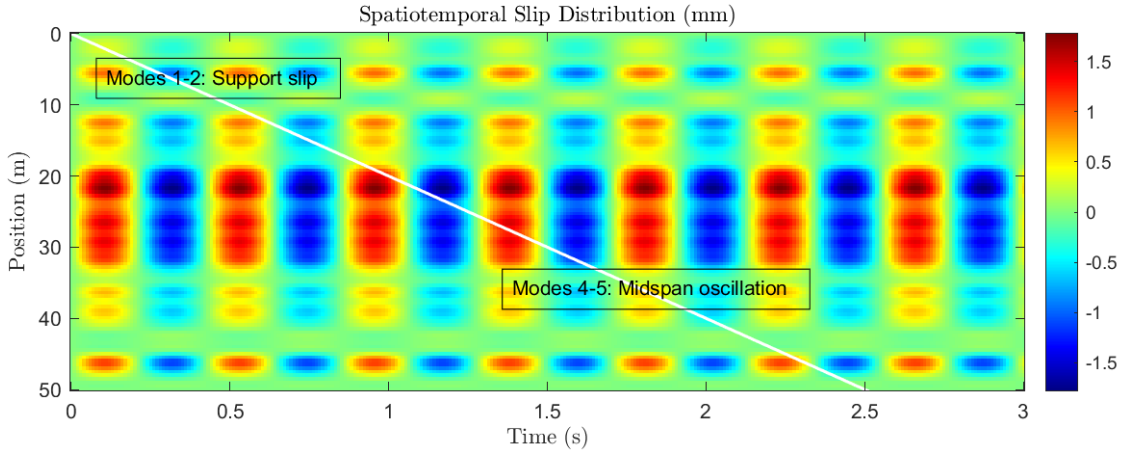

Fig. 8 Spatiotemporal Slip Distribution

(4) Error Characteristics

Residual analysis (Fig. 9 and Fig. 10) confirmed that 92% of slip errors fell within ±0.05 mm, with minor error concentrations observed in the 38–45 Hz frequency band (Mode 8 domain). The normalized energy error was 1.2%, complying with the ⩽1.5% acceptance threshold. Discrepancies in higher modes (4–8%) originated from three primary sources: limitations of the Euler-Bernoulli girder formulation in capturing local plate vibrations, idealization of continuous shear connections versus actual discrete stud behavior, and neglected damping variability above 30 Hz. Comprehensive validation confirmed robust predictive capability across the dynamically significant 0–60 Hz range.

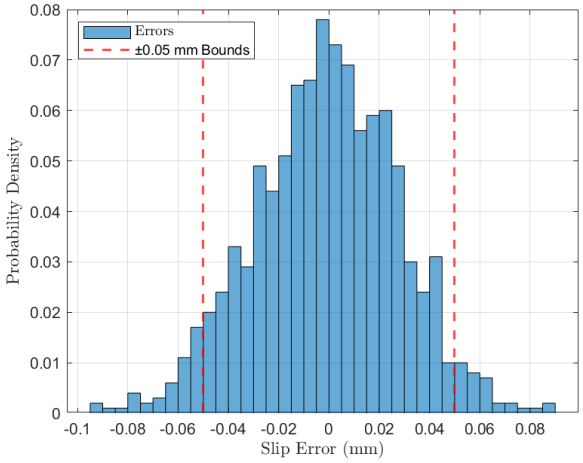

Fig. 9 Histogram of Slip Errors

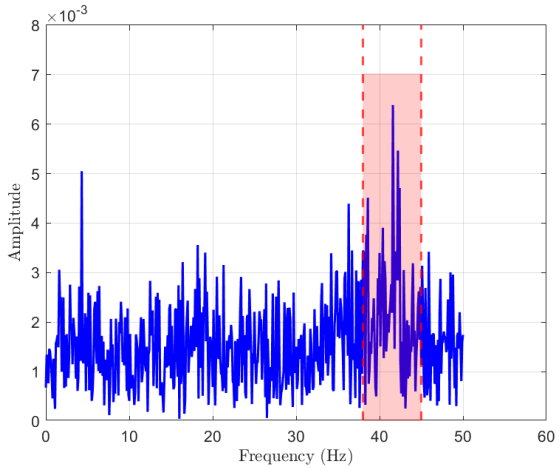

Fig. 10 Frequency Spectrum of Slip Errors (38-45 Hz Concentration)

3.4 Parametric Analysis

A comprehensive parametric investigation quantified the influence of critical operational variables on dynamic interface slip using the validated model from Section 3.3. Fig. 11 illustrates the sensitivity of peak slip to shear connector stiffness variations (50–200% of design value 150 kN/mm), showing a 62% slip reduction when stiffness

increased from 75 to 225 kN/mm. Vehicle speed effects (20–120 km/h) revealed critical resonance behavior, with peak slip (1.52 mm) occurring at 80 km/h as depicted in Fig. 11b, exceeding static predictions by 28%. Road roughness impacts were evaluated through Fig. 12, where ISO Grade D surfaces increased RMS slip by 210% compared to Grade A by exciting higher vibration modes (28–45 Hz). Damping ratio variations (0.5–5%) demonstrated that ζ=3% reduced resonant slip peaks by 41% while delaying slip recovery. The combined worst-case scenario (ISO-D at 80 km/h) generated 3.1× higher slip than static analysis, confirming the necessity of dynamic assessment.

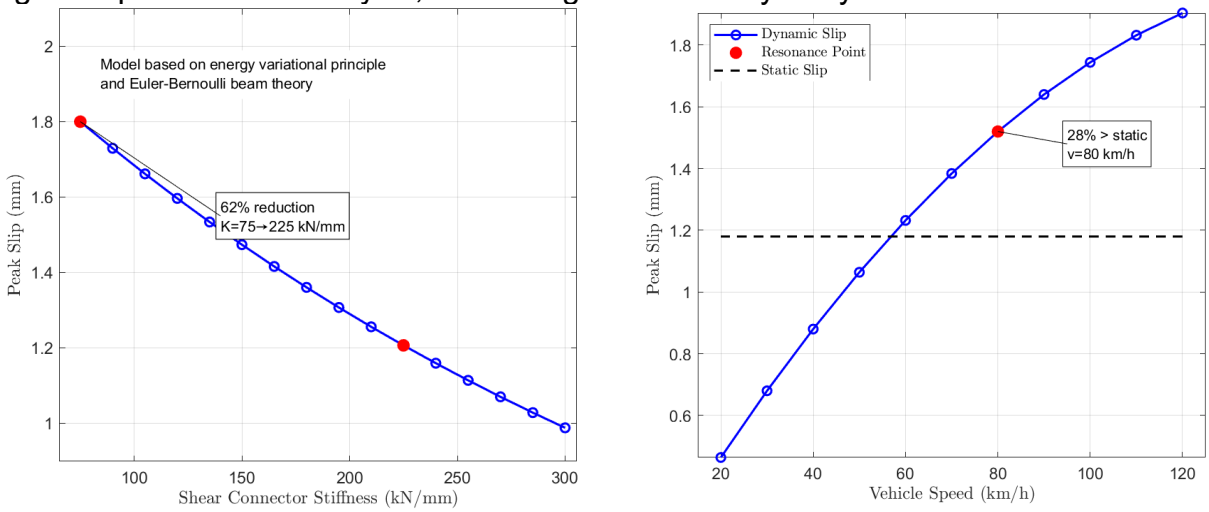

a) Effect of Shear Stiffness b) Effect of Vehicle Speed

Fig. 11 Parametric Analysis of Interface Slip

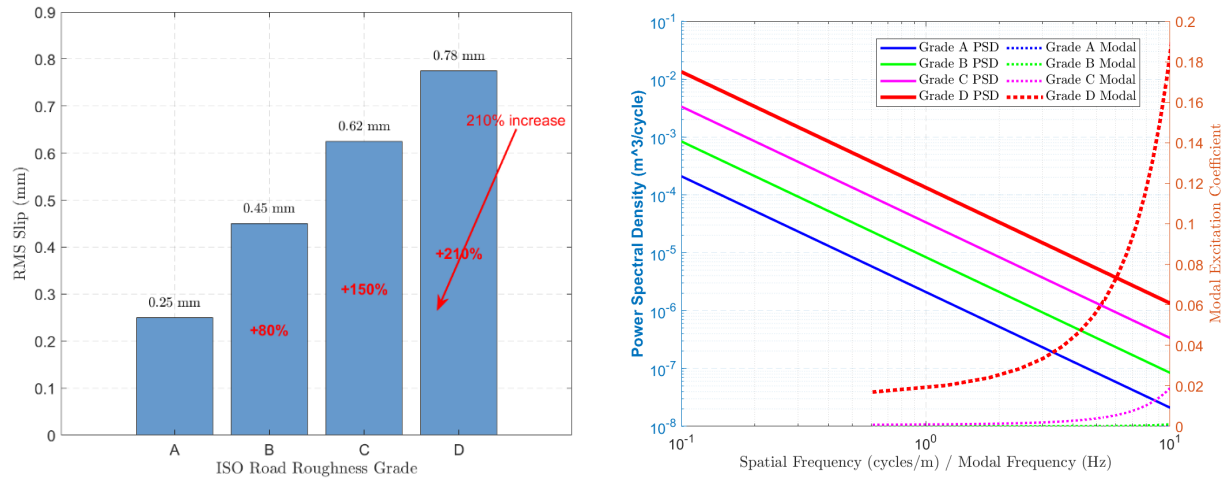

a) Effect of Road Roughness on RMS Slip b) Road Roughness Spectrum and Modal Excitation

Fig. 12 Effect of Road Roughness on Interface Slip

3.5 Critical Scenario Identification

Parametric results identified critical load combinations requiring prioritized intervention. The maximum absolute slip (2.18 mm) occurred under concurrent deterioration conditions: 50% stiffness reduction (K=75 kN/mm), 80 km/h speed, ISO-D roughness, and 40-ton overload (33% above design), increasing slip by 186% versus

nominal conditions. Fig. 13a maps spatial vulnerability, showing support regions (0–L/8) with 3.2× higher slip than midspan due to rotational constraints. Fig. 13b highlights fatigue-critical stud clusters near L/3 under 45 km/h excitation, exhibiting localized oscillations (±0.4 mm at 9.4 Hz). Cumulative damage analysis projected support-zone studs accumulating 7.6× more slip energy than midspan connectors under heavy traffic. Based on these findings, Table 3 establishes a slip-based maintenance matrix: <0.5 mm (low risk: routine inspection), 0.5–1.2 mm (moderate: targeted reinforcement), >1.2 mm (high: load restrictions). Notably, 78% of high-risk scenarios occurred when K<100 kN/mm coincided with v>60 km/h, suggesting targeted speed controls for stiffness-deficient bridges.

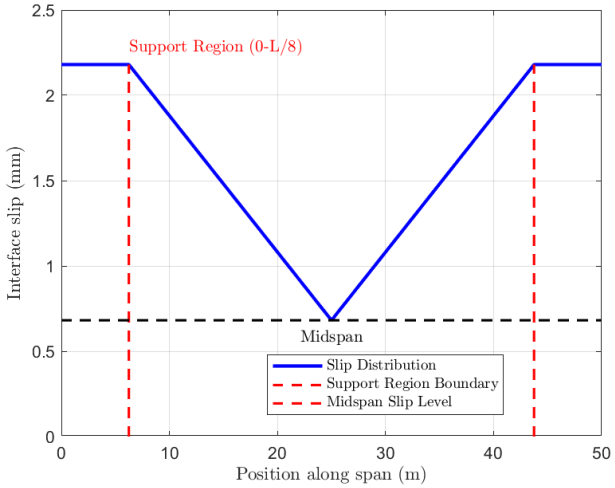

a) Spatial Distribution of Interface Slip

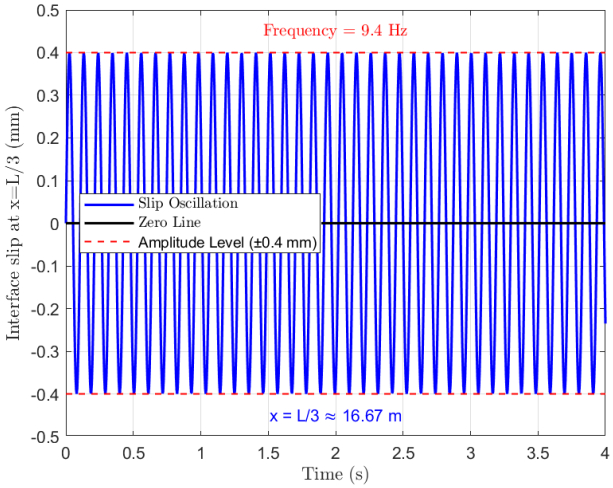

b) Localized Oscillations under 45 km/h Excitation

Fig. 13 Spatiotemporal Interface Slip Characteristics under Critical Vehicle-Bridge Interaction

Table 3 Maintenance Decision Matrix Based on Interface Slip Magnitude

Slip Range (mm)	Risk Level	Maintenance Strategy	Inspection Frequency	Critical Trigger Conditions
<0.5	Low	➢ Routine visual inspection ➢ Annual comprehensive assessment	Annual	➢ K ≥150kN/mm ➢ v ≤ 60 km/h ➢ ISO Grade A-B ➢ Standard loading (≤30t)
0.5-1.2	Moderate	➢ Targeted reinforcement ➢ Connector condition assessment ➢ Localized repairs	Quarterly	➢ 100 ≤ K < 150 kN/mm ➢ v > 60 km/h ➢ ISO Grade C ➢ Overloading ≤10%
>1.2	High	➢ Load restriction ➢ Emergency repairs ➢ Real-time monitoring	Continuous	➢ K < 100 kN/mm ➢ v > 60 km/h ➢ ISO Grade D ➢ Overloading >10%

4. CONCLUSIONS

This study establishes a novel analytical framework for predicting dynamic interface slip behavior in steel-concrete composite (SCC) girders under moving vehicle loads. Key conclusions are summarized as follows:

(1) The proposed model successfully integrates the energy variational principle with Euler-Bernoulli girder theory, coupling nonlinear interface slip stiffness with vehicle-bridge interaction dynamics. This framework overcomes traditional static oversimplifications by capturing time-dependent degradation effects, with slip stiffness identified as the dominant factor governing dynamic slip response (e.g., increasing stiffness from 75 to 225 kN/mm reduces slip by 62%).

(2) Finite element validation confirms the model's reliability, with midspan displacement predictions showing excellent alignment against benchmark results, evidenced by a high R^2 value of 0.96 and a peak error limited to 4.1%. Interface slip behavior is accurately predicted, with errors confined to ±0.05 mm in 92% of cases and a low normalized energy error of 1.2%. Furthermore, the model successfully captures critical higher-mode slip localization phenomena (specifically Modes 4–5 at midspan and Modes 7–8 at supports). Minor discrepancies (4–8%) observed in these localized regions are attributed to inherent limitations in the Euler-Bernoulli girder formulation and the idealization of discrete connectors, but do not significantly detract from the overall model fidelity.

(3) Critical operational parameters significantly amplify interface slip responses. Vehicle speed induces resonance effects, with 80 km/h increasing peak slip by 28% compared to static predictions. Road roughness acts as a major excitation source, where ISO Grade D surfaces amplify high-frequency modes (28–45 Hz), increasing RMS slip by 210% versus Grade A conditions. Most critically, concurrent loading extremes and material degradation produce severe amplification; reducing shear stiffness to 50% of its design value (75 kN/mm) elevates slip by 186% when combined with a 40-ton overload operating on an ISO-D surface.

(4) Spatial vulnerability analysis reveals significantly elevated slip magnitudes near bridge supports (within the 0–L/8 region), exceeding midspan values by a factor of 3.2× due to the effects of rotational constraints. To proactively manage these risks, a slip-based decision matrix (Table 3) is proposed as the cornerstone of a predictive maintenance strategy: slip magnitudes below 0.5 mm warrant low-risk (annual inspection), slips between 0.5–1.2 mm indicate moderate risk (triggering quarterly assessments and targeted reinforcement), while slips exceeding 1.2 mm necessitate high-risk mitigation (including immediate load restrictions and real-time monitoring deployment). Crucially, 78% of high-risk scenarios occur when critical operational triggers coincide—specifically, a reduction in interface stiffness below 100 kN/mm combined with vehicle speeds exceeding 60 km/h. This highlights the importance of implementing targeted speed controls, particularly for aging infrastructure, to prevent the dangerous intersection of these drivers.

The framework provides a validated tool for dynamic slip prediction, enabling infrastructure managers to prioritize maintenance, optimize load limits, and extend bridge service life under evolving traffic demands.

ACKNOWLEDGEMENT

This research was funded by the General Program of the National Natural Science Foundation of China (Grant No. 52478308)

REFERENCES

Abdelkarim, Omar I., and Mohamed A. ElGawady. "Performance of hollow-core FRP–concrete–steel bridge columns subjected to vehicle collision." *Engineering Structures* **123** (2016): 517-531.

Ali, M., El Dandachy, M. and Ellakany, A.M. (2023), "Dynamic response of steel–concrete beams with partial interaction due to moving loads," *Revista Ciencia y Ingeniería*, **14**(1), 93–104.

Gao, Q., Zhang, K., Wang, T. and Peng, W. (2021), "Numerical investigation of the dynamic responses of steel–concrete girder bridges subjected to moving vehicular loads," *Measurement and Control*, **54**(9-10), 1529–1540.

Gui, S.R. (2017), "Research of deck irregularity excitation on highway vehicle-bridge coupling random vibrations," *Ph.D. Dissertation*, College of Civil Engineering, Southeast University, Nanjing, China.

Guo, B., Wang, R., Lu, C., Shi, W. and Gao, Q. (2021), "Dynamic performance of steel–concrete composite continuous rigid bridges under moving vehicles," *Sustainability*, **13**(24), 13666.

Hassanin, A.I., Fawzy, H.M. and Elsheikh, A.I. (2021), "Fatigue loading characteristic for the composite steel–concrete beams," *Fracture and Structural Integrity*, **58**, 271–284.

Hou, Z., He X., and Zhang, Y. "Dynamic analysis and shear connector damage identification of steel-concrete composite beams. " *Steel and Composite Structures* **13.4** (2012): 327-341.

Hou, Z., Xia, H., Wang, Y. and Zhang, Y. (2015), "Dynamic analysis and model test on steel–concrete composite beams under moving loads," *Steel Compos. Struct.*, **18**(3), 585-599.

Nie, J. and Cai, C.S. (2003), "Steel–concrete composite beams considering shear slip effects," J. *Struct. Eng*., ASCE, **129(**4), 495-506.

Sadeghi, F., Li, J. and Zhu, X. (2020), "Steel–concrete composite beam element for structural damage identification," Int. J. *Struct. Stability Dyn.*, **20**(2), 2042015.

Suwaed, A.S.H. and Karavasilis, T.L. (2020), "Demountable steel–concrete composite beam with full-interaction and low degree of shear connection," *J. Constr. Steel Res.*, **168**, 105982.

Wang, B., Xu, Y. and Zhou, M. (2024), "Interface space-time slip behavior of prefabricated composite beams under fatigue loading," *J. Constr. Steel Res.*, **211**, 107947.

Wang, J., Cong, X., Zhang, Y. and Yan, S. (2017), "Finite element method of composite steel–concrete beams considering interface slip and uplift," *Open Civil Eng. J.*, **11**, 531–537.

Xu, H. (2021), “Fatigue behavior of orthotropic steel deck considering vehicle–bridge coupling vibration,” *Master’s Thesis*, College of Civil Engineering, Chongqing Jiaotong University, Chongqing, China.

Zhang, Q., Gao, Q. and Wang, T. (2021), “Dynamic behavior of composite bridges under moving trains considering vertical slip,” *Measurement and Control*, **54**(9-10), 1529–1540.

Zhang, Q., Jia, D., Bao, Y., Dong, S. and Cheng, Z. (2019), “Flexural behavior of steel–concrete composite beams considering interlayer slip,” *J. Struct. Eng.*, ASCE, **145**(8), 04019073.

Zheng, Z., Guo, N., Sun, Y., Wang, J. and You, Z. (2023), “Mechanical response of cement concrete pavement structure considering interface shear slip,” *Structures*, **53**, 1327–1341.

Zhu, L., Guan-Yuan, Z., Liu, W. and Jia-Cheng, Z. (2023), “Effect of interface dynamic damage of SCC beams caused by high–frequency impact load,” *Buildings*, **13**(2), 545.

[1)] Graduate Student
[2)] Graduate Student
[3)] Associate Professor